



## **VLBI Observations of Supernova PTF11qcj: Direct Constraints on the Size of the Radio Ejecta**

Downloaded from: <https://research.chalmers.se>, 2025-12-04 22:44 UTC

Citation for the original published paper (version of record):

Palliyaguru, N., Corsi, A., Perez-Torres, M. et al (2021). VLBI Observations of Supernova PTF11qcj: Direct Constraints on the Size of the Radio Ejecta. *Astrophysical Journal*, 910(1).  
<http://dx.doi.org/10.3847/1538-4357/abe1c9>

N.B. When citing this work, cite the original published paper.



# VLBI Observations of Supernova PTF11qej: Direct Constraints on the Size of the Radio Ejecta

N. T. Palliyaguru<sup>1</sup>, A. Corsi<sup>1</sup>, M. Pérez-Torres<sup>2</sup>, E. Varenius<sup>3,4</sup>, and H. Van Eerten<sup>5</sup>

<sup>1</sup> Department of Physics and Astronomy, Texas Tech University, Lubbock, TX 79409-1051, USA; [Nipuni.Palliyaguru@ttu.edu](mailto:Nipuni.Palliyaguru@ttu.edu)

<sup>2</sup> Instituto de Astrofísica de Andalucía-Consejo Superior de Investigaciones Científicas (CSIC), P.O. Box 3004, E-18008, Granada, Spain

<sup>3</sup> Department of Earth and Space Sciences, Chalmers University of Technology, Onsala Space Observatory, SE-439 92 Onsala, Sweden

<sup>4</sup> Jodrell Bank Centre for Astrophysics, The University of Manchester, Oxford Rd, Manchester M13 9PL, UK

<sup>5</sup> Department of Physics, University of Bath, Claverton Down, Bath BA2 7AY, UK

Received 2020 December 31; revised 2021 January 29; accepted 2021 January 29; published 2021 March 23

## Abstract

We present High Sensitivity Array and enhanced Multi-Element Remotely Linked Interferometer Network observations of the radio-loud broad-lined Type Ic supernova PTF11qej obtained  $\sim 7.5$  yr after the explosion. Previous observations of this supernova at 5.5 yr since explosion showed a double-peaked radio light curve accompanied by a detection in the X-rays, but no evidence for broad  $H\alpha$  spectral features. The Very Long Baseline Interferometry (VLBI) observations presented here show that the PTF11qej GHz radio ejecta remains marginally resolved at the submilliarcsecond level  $\approx 7.5$  yr after the explosion, pointing toward a nonrelativistic expansion. Our VLBI observations thus favor a scenario in which the second peak of the PTF11qej radio light curve is related to the strong interaction of the supernova ejecta with a circumstellar medium of variable density, rather than to the emergence of an off-axis jet. Continued VLBI monitoring of PTF11qej in the radio may further strengthen this conclusion.

*Unified Astronomy Thesaurus concepts:* Type Ic supernovae (1730); Very long baseline interferometry (1769); Gamma-ray bursts (629); Stellar astronomy (1583)

## 1. Introduction

Supernovae (SNe) of Type Ib/c are believed to mark the deaths of massive stars that are stripped of their hydrogen (Type Ib), and possibly helium (Type Ic), envelope before explosion (Filippenko 1997). A subclass of Ib/c SNe dubbed broad-line (BL) Ic, estimated to constitute only  $\approx 5\%$  of the Ib/c population (Woosley & Bloom 2006; Gal-Yam 2017), is of particular interest due to its relation to long-duration gamma-ray bursts (GRBs), the most relativistic stellar explosions we know of in the universe (Piran 2004; Mészáros 2006). While all GRB-associated SNe are of Type BL-Ic (Woosley & Bloom 2006; Hjorth & Bloom 2012, but see Cano et al. 2014 for the peculiar case of SN 2013ez), not all BL-Ic events make a GRB (e.g., Berger et al. 2003; Soderberg et al. 2006; Corsi et al. 2016). Thus, the question of what physical ingredients enable some stripped-envelope massive stars to launch a relativistic jet remains open (e.g., Modjaz et al. 2016).

As first demonstrated by the well-known case of SN 1998bw/GRB 980425 (Galama et al. 1998; Kulkarni et al. 1998), radio observations are particularly well suited for identifying those BL-Ic SNe that may harbor GRBs (hereafter referred to as engine-drive SNe), because radio synchrotron emission traces the fastest-moving ejecta (e.g., Berger et al. 2003). At the same time, because nonthermal radio photons are produced in the interaction of the SN shock with the circumstellar material (CSM), bright radio emission can also be the smoking gun for (nonrelativistic) ejecta interacting with a high-density CSM (e.g., Chevalier 1998; Chevalier et al. 2004; Chevalier & Fransson 2006). Although strong CSM

interaction is not commonly observed in BL-Ic SNe, a few cases exist such as SN 2007bg (Salas et al. 2013), PTF11qej (Corsi et al. 2014; Palliyaguru et al. 2019), SN 2018gep (Ho et al. 2019a), and possibly, AT 2018cow (Rivera Sandoval et al. 2018; Smartt et al. 2018; Ho et al. 2019b; Margutti et al. 2019).

Here, we focus on PTF11qej, a radio-loud BL-Ic SN extensively monitored via our approved programs on the Karl G. Jansky Very Large Array (VLA; Corsi et al. 2014; Palliyaguru et al. 2019). The extraordinary radio luminosity of PTF11qej ( $\sim 10^{29}$  erg s $^{-1}$  Hz $^{-1}$ ) is reminiscent of the GRB-associated SN 1998bw (Kulkarni et al. 1998). As discussed in Corsi et al. (2014) and Palliyaguru et al. (2019), our radio monitoring over the first  $\approx 5.5$  yr since explosion has revealed an unusual double-peaked radio light curve. The radio emission observed during the first light-curve peak ( $t \lesssim 200$  days) can be modeled within the standard synchrotron self-absorption (SSA) model for a spherical SN shock expanding in the CSM. This model yields an estimated speed of  $\approx 0.3c$ – $0.5c$  for the fastest SN ejecta (Corsi et al. 2014), placing PTF11qej in an intermediate class between “ordinary” BL-Ic SNe and engine-driven ones like SN 1998bw or SN 2009bb (Soderberg et al. 2010). The simple, spherically symmetric model of SN shock interaction with a smooth CSM (simple power-law density profile), however, cannot explain the second radio peak. As discussed in Palliyaguru et al. (2019), two more complex scenarios can be invoked to interpret this peculiar behavior of PTF11qej: (i) a spherical SN shock going through a medium with extreme CSM density variations, perhaps related to eruptive progenitor mass loss, and (ii) a radio-emitting SN shock (first peak) followed by radio emission from an emerging off-axis GRB jet, initially pointed away from our line of sight (second peak).



Original content from this work may be used under the terms of the [Creative Commons Attribution 4.0 licence](https://creativecommons.org/licenses/by/4.0/). Any further distribution of this work must maintain attribution to the author(s) and the title of the work, journal citation and DOI.

In Palliyaguru et al. (2019), we have shown that, while modeling of our VLA data set within scenario (i) can indeed explain the second radio peak, the presence of an off-axis jet (scenario (ii)) cannot be ruled out just based on light-curve measurements. However, scenarios (i) and (ii) make rather different predictions for the angular size of the PTF11qej ejecta at very late times. Motivated by these considerations, here we present Very Long Baseline Interferometry (VLBI) observations of PTF11qej aimed at setting direct constraints on the size (angular diameter) of its radio ejecta. These observations ultimately provide a direct test for the presence of relativistic expansion, as expected in the case of an off-axis GRB jet.

Our paper is organized as follows. In Section 2, we present the High Sensitivity Array (HSA) and enhanced Multi-Element Remotely Linked Interferometer Network (eMERLIN) observations of PTF11qej. In Section 3, we discuss these observations within the light curve and radio ejecta size predictions of the two scenarios mentioned above. Finally, in Section 4, we summarize our results and conclude.

## 2. Observations and Data Reduction

### 2.1. HSA Observations

We observed the field of PTF11qej at 1.66 GHz (project code BP229A, PI: Palliyaguru) and 15.37 GHz (BP229B, PI: Palliyaguru) with the HSA on 2018 December 08.37 UTC and 2019 April 28.97 UTC. The HSA included, in both bands, the Very Long Baseline Array (VLBA; USA) and the Effelsberg 100 m antenna (Germany). At 1.66 GHz, we also used the VLA for improved sensitivity. Both observations covered the 128 MHz continuum bandwidth and were correlated at the National Radio Astronomy Observatory (NRAO) Array Operations Center in Socorro (New Mexico, USA) with averaging times of 2 s and 1 s at 1.66 GHz and 15.37 GHz, respectively. In both observations, we correlated the target data at R.A.  $13^{\text{h}}13^{\text{m}}41^{\text{s}}.5100$ , decl.  $+47^{\circ}17'57''.600$  (J2000; Corsi et al. 2014). In setting up our observations, we used standard phase referencing, where scans on target are interleaved with scans on a nearby compact complex gain calibrator with known position. At 1.66 GHz and 15.37 GHz, we used J1310+4653 and J1358+4737, respectively, as our complex gain calibrators. The VLBA observations were correlated using the NRAO’s implementation of the DiFX software correlator (Deller et al. 2011).

We performed all calibration and imaging procedures using the 31DEC19 release of the Astronomical Image Processing System (Greisen 2003) and Parsel–Tongue (Kettenis et al. 2006). PTF11qej was clearly detected at both frequencies. At 1.66 GHz, in particular, given the relatively large separation between PTF11qej and the complex gain calibrator J1358+4737 ( $\approx 7''.6$ ), we used self-calibration to correct for the residual phase errors toward PTF11qej and obtain a reliable flux density measurement. The final VLBI images are presented in Figure 1.

We fitted Gaussian intensity profiles to the target images to obtain the flux density and position of PTF11qej at each frequency. Our results are summarized in Table 1. The reported flux density uncertainties are the quadrature sum of the instrumental calibration uncertainty plus the uncertainty of the Gaussian fit. At 15.37 GHz, we adopt an instrumental uncertainty of 15%. At 1.66 GHz, we use an uncertainty of

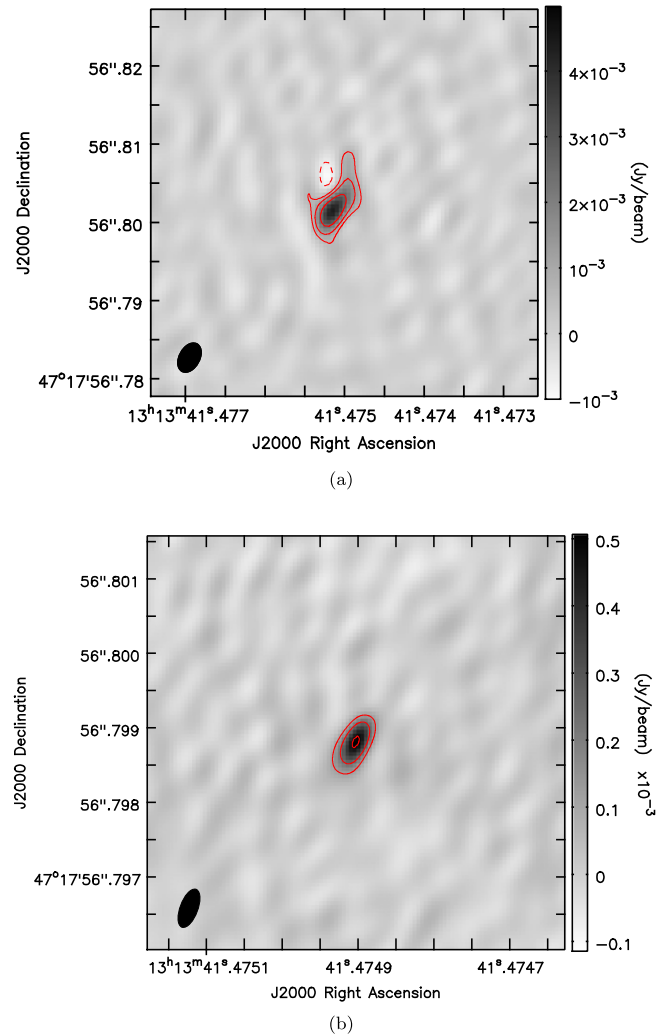


**Figure 1.** VLBI images of PTF11qej at 1.66 GHz (top) and 15.37 GHz (bottom). Note the different scales on the axes. For each plot, the contours are  $(-5, 5, 10, 20)$  times the rms noise given in Table 1.

**Table 1**  
HSA Results for PTF11qej (Project Codes BP229A and BP229B)

|   | 1.66 GHz  | 15.37 GHz                                       |
|---|---|---|
| Observing date (UT)                                     | 2018-12-08                                      | 2019-04-28                                      |
| Project code  | BP229A  | BP229B  |
| Observing time including calibrators (hr)               | 8   | 8   |
| Image off-source rms noise ( $\mu\text{Jy beam}^{-1}$ ) | 125   | 24  |
| CLEAN restoring beam ( $\text{mas}^2$ )                 | $4.06 \times 2.66$                              | $0.54 \times 0.24$                              |
| CLEAN beam position angle (deg)                         | $-29$   | $-21$   |
| Peak flux density (mJy)                                 | $4.32 \pm 0.92$                                 | $0.494 \pm 0.054$                               |
| Integrated flux density (mJy)                           | $5.8 \pm 1.4$                                   | $0.681 \pm 0.085$                               |
| R.A. [J2000]  | $13^{\text{h}}13^{\text{m}}41^{\text{s}}.47512$ | $13^{\text{h}}13^{\text{m}}41^{\text{s}}.47490$ |
| Decl. [J2000]   | $+47^{\circ}17'56''.8017$                       | $+47^{\circ}17'56''.7988$                       |
| Deconvolved fitted major axis                           | ...   | $300 \pm 71 \mu\text{arcsec}$                   |
| Deconvolved fitted minor axis                           | ...   | $76 \pm 76 \mu\text{arcsec}$                    |
| Deconvolved fitted Pos. ang.                            | ...   | $125^{\circ} \pm 19^{\circ}$                    |

**Note.** See Section 2.1 for discussion.

**Table 2**  
eMERLIN Results for PTF11qej (Project Code DD8011)

|   | 1.5 GHz  | 5.07 GHz                                       |
|---|--|--|
| Observing date (UT)                                     | 2019-08-29                                     | 2019-08-01                                     |
| Project code  | DD8011   | DD8011   |
| Observing time including calibrators (hr)               | 6  | 5  |
| Image off-source rms noise ( $\mu\text{Jy beam}^{-1}$ ) | 42   | 37   |
| CLEAN beam ( $\text{mas}^2$ )                           | $59 \times 19$                                 | $622 \times 78$                                |
| CLEAN beam position angle (deg)                         | 40   | 42   |
| Peak flux density (mJy)                                 | $5.82 \pm 0.87$                                | $4.15 \pm 0.62$                                |
| Integrated flux density (mJy)                           | $5.78 \pm 0.87$                                | $4.45 \pm 0.67$                                |
| R.A. [J2000]  | $13^{\text{h}}13^{\text{m}}41^{\text{s}}.4745$ | $13^{\text{h}}13^{\text{m}}41^{\text{s}}.4746$ |
| Decl. [J2000]   | $+47^{\circ}17'56''.795$                       | $+47^{\circ}17'56''.800$                       |

**Note.** See Section 2.2 for discussion.

20% to also account for residual errors due to the large separation between the target and the complex gain calibrator.

To estimate the source size, we fit Gaussian intensity distributions to the images. We find that the source appears marginally resolved along the major axis of our 15.37 GHz observations, while the minor axis is consistent with an unresolved source. The deconvolved major (minor) FWHM size of the fitted Gaussian model is  $300 \pm 71 \mu\text{as}$  ( $76 \pm 76 \mu\text{as}$ ), with a position angle of  $125^\circ \pm 19^\circ$  (see also Table 1). This corresponds to a diameter of  $(5.2 \pm 1.2) \times 10^{17}$  cm ( $(1.3 \pm 1.3) \times 10^{17}$  cm). Given the relatively weak radio emission from PTF11qej, although this result gives us an estimate of the source size, we refrain from speculating about the nonsymmetrical nature of this result. The radio ejecta of PTF11qej is not resolved at 1.66 GHz. We note an apparent positive extension in Figure 1(a), but also a significant negative peak nearby. Such an asymmetry is very likely due to residual phase errors, even after self-calibration, caused by the significant separation between target and complex gain calibrator in BP229A. We, therefore, refrain from further interpretation of this  $5\sigma$  level structure.

## 2.2. eMERLIN Observations

We observed the field of PTF11qej at 5.07 GHz and 1.51 GHz with all six eMERLIN antennas on 2019 August 01.55 UTC and 2019 August 29.47 UTC via our DDT project DD8011 (PI: Perez-Torres). We used J1310+4653 as our complex gain calibrator, 1 s integration time, and 512 MHz continuum bandwidth in both bands. We used the standard eMERLIN calibrators 3C 286 and OQ 208 for flux density calibration and bandpass calibration, respectively.

We calibrated and edited the correlated data using the eMERLIN CASA pipeline version 1.1.11 (Moldon 2018). We applied self-calibration in both bands to correct for significant residual phase errors and minor amplitude errors. We used WSClean (Offringa et al. 2014) to deconvolve the calibrated data and produce the final images. PTF11qej is clearly detected in both bands.

We report in Table 2 the peak and total flux densities, along with the position, of PTF11qej, at each frequency, calculated by fitting Gaussian intensity profiles to the images. The quoted flux density uncertainties correspond to the sum in quadrature

of the systematic, i.e., instrumental uncertainty (15%) and the image off-source rms noise.

## 3. Modeling

The complete radio light curves of PTF11qej are shown in Figure 2. These include the latest flux measurements (integrated fluxes from Tables 1 and 2) along with data published in Corsi et al. (2016) and Palliyaguru et al. (2019). Hereafter, we discuss the possible interpretation of these light curves within the standard SSA scenario for radio SNe (see Soderberg et al. 2005 and references therein). We also consider an alternative interpretation within an SSA (the first radio light-curve peak) plus off-axis GRB (the second radio light-curve peak) scenario. Finally, we discuss the direct size constraints obtained via our VLBI observations in the context of both these scenarios.

### 3.1. Light Curves within the SSA Scenario

Similarly to what was done in Corsi et al. (2016) and Palliyaguru et al. (2019), we can model the radio emission of PTF11qej in the SSA scenario (Soderberg et al. 2005). As described in Soderberg et al. (2005), the temporal evolution of the shock radius,  $r$ , minimum Lorentz factor,  $\gamma_m$ , and magnetic field,  $B$ , are parameterized as

$$r = r_0 \left( \frac{t - t_e}{t_0} \right)^{\alpha_r}, \quad (1)$$

$$B = B_0 \left( \frac{t - t_e}{t_0} \right)^{\alpha_B}, \quad (2)$$

$$\gamma_m = \gamma_{m,0} \left( \frac{t - t_e}{t_0} \right)^{\alpha_\gamma}, \quad (3)$$

with  $\alpha_r$ ,  $\alpha_B$ , and  $\alpha_\gamma$  the temporal indices of the three quantities, respectively;  $t_e$  the explosion time, and  $t_0$  an arbitrary reference epoch since explosion, here set to 10 days. Within the standard assumptions, one has (see Equations (9)–(10) in Soderberg et al. 2005)

$$\alpha_\gamma = 2(\alpha_r - 1), \quad (4)$$

$$\alpha_B = \frac{(2 - s)}{2} \alpha_r - 1. \quad (5)$$

Here,  $s$  describes the density profile of the shocked CSM where the density of the radiating electrons within the shocked CSM is given by (Chevalier 1982)

$$n_e = n_{e,0} \left( \frac{t - t_e}{t_0} \right)^{\alpha_{n_e,0}} \propto r^{-s}. \quad (6)$$

The above relations follow from assuming that the energy density of shocked particles (protons and electrons) and amplified magnetic fields are a constant fraction ( $\epsilon_e \approx \epsilon_B \approx 0.33$  under the hypothesis of equipartition) of the postshock energy density  $U \propto n_e v^2$ , where

$$v = v_0 \left( \frac{t - t_e}{t_0} \right)^{\alpha_r - 1} \quad (7)$$

is the shock speed. The density of electrons in the shocked CSM is related to the progenitor mass-loss rate via the relation

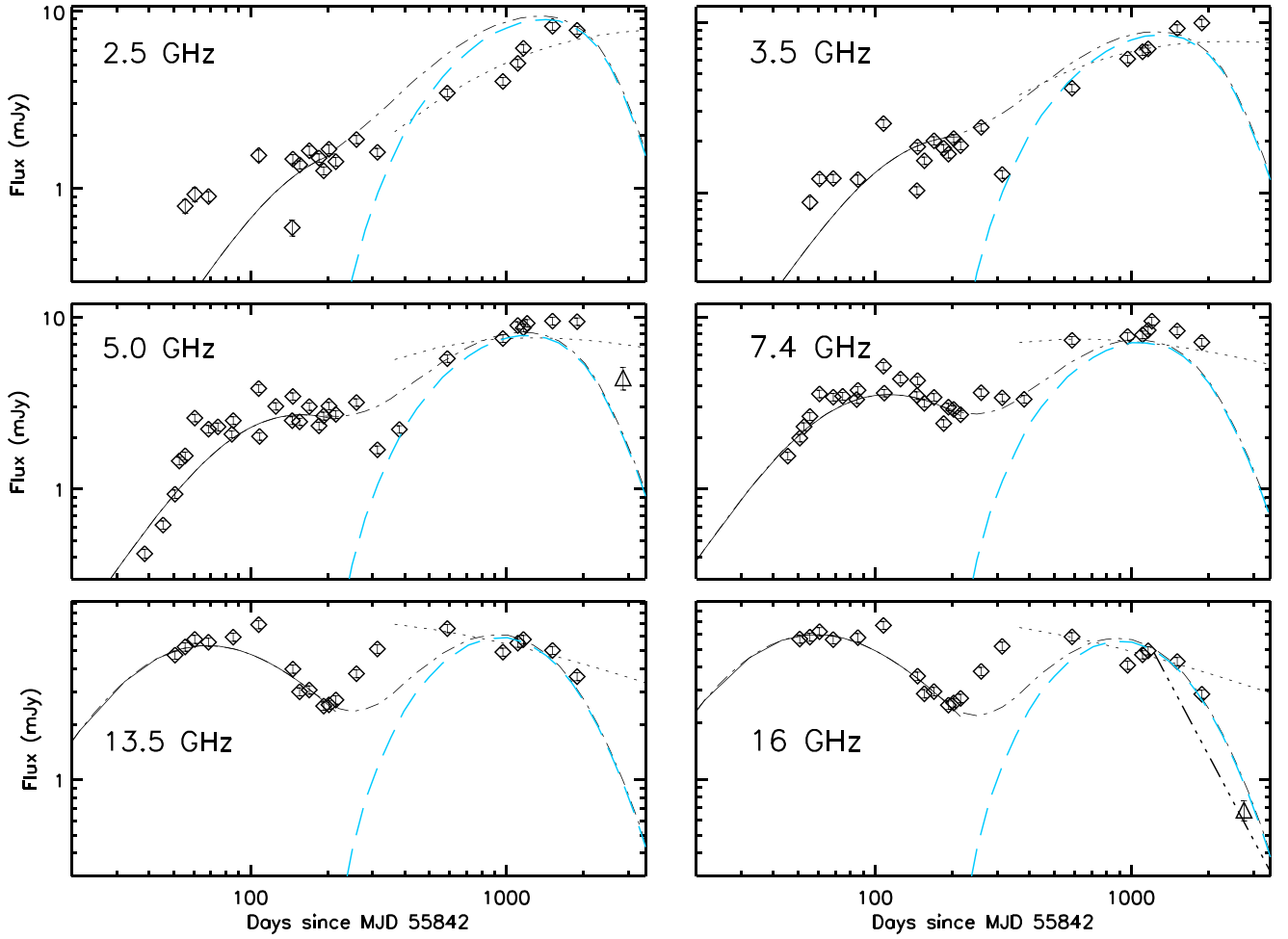


**Figure 2.** Radio light curves of PTF11qej obtained with the VLA, HSA, and eMERLIN at six different frequencies. The latest HSA and eMERLIN data are shown by triangles. The first radio peak is modeled within a standard SSA model as described in Corsi et al. (2014; Model 0 in Table 3; solid curves). The rebrighening phase is modeled in two different scenarios: (i) within the standard SSA model (dotted curves; Model 3 in Table 3) and (ii) within an off-axis afterglow model (long-dashed, blue curves; see Section 3.2). The sum of the best-fit CSM model in the first peak and off-axis jet emission from the second peak is also shown (dotted–dashed curve). The dashed–triple-dotted line in the bottom-right panel shows the effects of synchrotron cooling within the SSA scenario as discussed in Section 3.1. The measurement of the shock size from HSA data rules out the off-axis jet scenario.

(see Equation (13) in Soderberg et al. 2005)

$$\dot{M} = \frac{8\pi n_{e,0} m_p r_0^2 v_w}{\eta} \left( \frac{t - t_e}{t_0} \right)^{\alpha_r(2-s)} = \dot{M}_0 \left( \frac{t - t_e}{t_0} \right)^{\alpha_M}, \quad (8)$$

where we have assumed a nucleon-to-proton ratio of 2,  $v_w \sim 1000 \text{ km s}^{-1}$  is the velocity of the stellar wind, and where  $\eta$  (typically in the range  $\eta \sim 2\text{--}10$ ) characterizes the thickness of the radiating electron shell as  $r/\eta$ .

In the GHz radio band, the observing frequencies  $\nu$  are typically such that  $\nu_m \ll \nu$ , where (see Equation (A6) in Soderberg et al. 2005)

$$\nu_m = \gamma_m^2 \left( \frac{eB}{2\pi m_e c} \right) \quad (9)$$

is the characteristic synchrotron frequency of electrons with Lorentz factor  $\gamma_m$ . In the above equation,  $m_e$  is the electron mass, and  $c$  is the speed of light. In this frequency range, assuming the synchrotron cooling frequency is higher than the observing frequency, and ignoring synchrotron cooling effects,

the SSA emission from the shocked electrons reads

$$f_\nu(t) = \mathcal{F} \left( \frac{t - t_e}{t_0} \right)^{(4\alpha_r - \alpha_B)/2} (1 - e^{-\tau_\nu(t)})^{1/\xi} \nu^{5/2}, \quad (10)$$

where  $\mathcal{F}$  is a normalization constant that depends on the parameters ( $r_0$ ,  $B_0$ ,  $p$ ) with  $p$  the power-law index of the electron energy distribution (see Equations (A11)<sup>6</sup> and (A13) in Soderberg et al. 2005), and where the optical depth  $\tau$  is given by (see Equations (20) and (A14) in Chevalier & Fransson 2003; Soderberg et al. 2005, respectively)

$$\tau(t) = \mathcal{T} \left( \frac{t - t_e}{t_0} \right)^{(p-2)\alpha_\gamma + (3+p/2)\alpha_B + \alpha_r} \nu^{-(p+4)/2}, \quad (11)$$

with  $\mathcal{T}$  a normalization constant that depends on the parameters ( $r_0$ ,  $B_0$ ,  $p$ ,  $\gamma_{m,0}$ ,  $\eta$ ). We note that for  $\nu_m \ll \nu$ , the value of  $\gamma_{m,0}$  is left largely unconstrained by the observations and thus typically fixed so that  $\nu_{m,0} \sim 1 \text{ GHz}$ . In addition, the thickness of the shell is typically set to a value  $\eta > 1$  (Li &

<sup>6</sup> The functions defined in Equation (A11) of Soderberg et al. (2005) are not time dependent and therefore included in the normalization constant.

**Table 3**  
Best-fit Parameters for the Standard SSA Model Described in Section 3.1

| Parameter                            | Model 0              | Model 1                         | Model 2                         | Model 3                         |
|--------------------------------------|----------------------|---------------------------------|---------------------------------|---------------------------------|
| $r_0$ (cm)                           | $1.1 \times 10^{16}$ | $1.1 \times 10^{16}$<br>(fixed) | $1.1 \times 10^{16}$<br>(fixed) | $1.1 \times 10^{16}$<br>(fixed) |
| $\xi$                                | 0.23                 | 0.19                            | 0.19                            | 0.34                            |
| $\alpha_r$                           | 0.79                 | 0.79 (fixed)                    | 0.79 (fixed)                    | 0.61                            |
| $t_e$                                | 55842 (fixed)        | 55842<br>(fixed)                | 55842<br>(fixed)                | 55842<br>(fixed)                |
| $s$                                  | 2.0 (fixed)          | 1.4                             | 1.1                             | 0.0 (fixed)                     |
| $B_0$ (G)                            | 6.7                  | 5.8                             | 3.2                             | 1.35                            |
| $p$                                  | 3.0 (fixed)          | 3.0 (fixed)                     | 3.0 (fixed)                     | 3.0 (fixed)                     |
| $\alpha_B$                           | -1.0                 | -0.76                           | -0.64                           | -0.39                           |
| $\gamma_{m,0}$                       | 7.3                  | 7.8                             | 10.5                            | 28.1                            |
| $\alpha_\gamma$                      | -0.4                 | -0.4                            | -0.4                            | -0.8                            |
| $n_{e,0}$ (cm $^{-3}$ )              | $1.5 \times 10^5$    | $1.0 \times 10^5$               | $2.4 \times 10^4$               | $1.6 \times 10^3$               |
| $\alpha_{n_e}$                       | -1.6                 | -1.1                            | 1-0.88                          | 0.0                             |
| $\dot{M}_0$ ( $M_\odot$ yr $^{-1}$ ) | $1.2 \times 10^{-4}$ | $8.4 \times 10^{-5}$            | $1.9 \times 10^{-5}$            | $6.4 \times 10^{-6}$            |
| $\alpha_{\dot{M}}$                   | 0.0                  | 0.48                            | 0.71                            | 1.2                             |
| $\chi^2/\text{dof}$                  | 1793/90              | 1288/39                         | 602/38                          | 211/38                          |

Chevalier 1999). Thus, for a given choice of  $\eta$  and  $\nu_m$ , the SSA model is a function of the parameters ( $r_0$ ,  $\xi$ ,  $\alpha_r$ ,  $t_e$ ,  $s$ ,  $B_0$ ,  $p$ ).

Within the SSA scenario and with the data collected here, we can further test the hypothesis first presented in Palliyaguru et al. (2019) that the double-peaked radio light curve of PTF11qj is due to the strong interaction with CSM of variable density. Our results are shown in Figure 2 and are reported in Table 3. Model 0 in Table 3 is the best-fit SSA model for the first peak ( $t \lesssim 215$  days since explosion) as reported in Corsi et al. (2016). The last is obtained by setting  $t_e = 55842$ ,  $p = 3$  (as typically expected for Type Ib/c SNe; see Chevalier & Fransson 2006),  $\eta = 10$ , and  $\nu_{m,0} = 1$  GHz, and varying  $r_0$ ,  $\xi$ ,  $\alpha_r$ ,  $s$ , and  $B_0$ . Model 0 is also plotted in Figure 2 (solid line). Model 1 is a fit to the second radio peak ( $t \gtrsim 587$  days since explosion) where we keep  $r_0$  and  $\alpha_r$  fixed to their best-fit values for the first peak so as to ensure a smooth radial evolution between the first and second radio light-curve peaks, and allow  $\xi$ ,  $s$ , and  $B_0$  to vary. This fit is similar to the one reported in Palliyaguru et al. (2019) but updated to include the eMERLIN and HSA data presented here.

Compared to Palliyaguru et al. (2019), the reduced  $\chi^2$  for Model 1 is substantially higher, indicating a worsening of the goodness of fit. Model 2 is a fit with a model identical to Model 1 but where the 15 GHz HSA data have been excluded. The improved  $\chi^2$  value for Model 2 compared to Model 1 indicates a significant discrepancy between data and model at the highest radio frequencies, suggesting a steepening in the highest frequency light curve, which may be caused by the passage of the cooling frequency in the band. Indeed, the effects of synchrotron cooling may become important at the late time-scales considered here. Within the SSA scenario, the synchrotron cooling frequency can be written as (see Equation (A16) in Soderberg et al. 2005)

$$\nu_c = \frac{18\pi m_e c e}{(t - t_e)^2 \sigma_T^2 B^3}, \quad (12)$$

where  $\sigma_T$  is the Thomson cross section and  $e$  is the electron charge (Rybicki & Lightman 1986; Soderberg et al. 2005). For

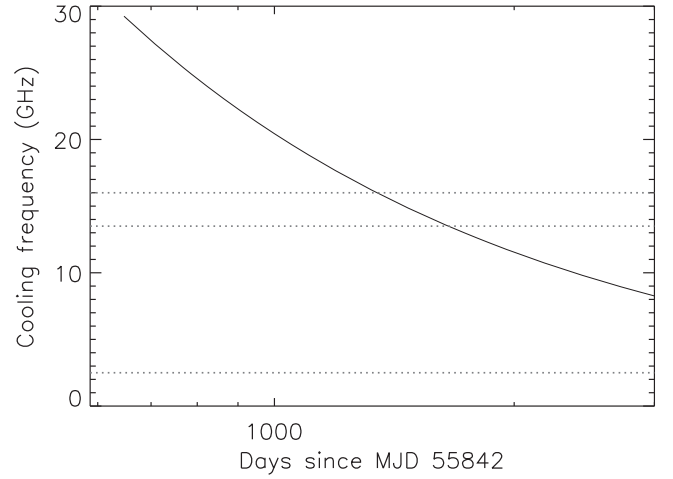


**Figure 3.** Cooling frequency vs. time during phase 2. The horizontal dotted lines mark the observation frequencies of 2.5, 13.5, and 16 GHz. For  $\alpha_r = 0.61$ ,  $\nu_{m,0} = 3$  GHz, and  $\eta = 2$  (Model 3),  $\nu_c$  (solid line) crosses 16 GHz at  $\sim 1345$  days since explosion.

$\nu > \nu_c$ , the flux density becomes (Soderberg et al. 2005)

$$f_\nu(t) \propto \nu^{-p/2} t^{(6\alpha_r + (8-5p)\alpha_B + 2(p-2)\alpha_\gamma - 4p + 2)/2}. \quad (13)$$

Model 1 in Table 3 predicts  $\nu_c \approx 50$  GHz at  $t - t_e \approx 7.5$  yr, which is above the highest frequency of our observations, resulting in large residuals with the HSA data point. Thus, in Table 3, we also report the results of a fit where we set  $t_e = 55842$ ,  $p = 3$ ,  $s = 0$ ,  $\eta = 2$ ,  $\nu_{m,0} = 3$  GHz, and  $r_0 = 1.1 \times 10^{16}$  cm, but allow  $\alpha_r$ ,  $B_0$ , and  $\xi$  to vary (Model 3). As shown in Figure 3, with this choice the cooling frequency falls below 16 GHz at  $t - t_e \approx 1345$  days ( $\approx 3.6$  yr since explosion), thus causing a steepening of the light curve at this frequency. In Figure 2, we plot Model 3 with dotted lines, and the expected steepening ( $f_\nu(t) \propto t^{-2.6}$  according to Equation (13)) of the 16 GHz light curve due to synchrotron cooling with a dashed-triple-dotted line. Model 3 substantially improves the goodness of fit for the second radio peak compared to Models 1 and 2.

In summary, while the SSA fits described in this section have large limitations due to the simplifications that characterize the SSA model, overall they are indicative of the fact that (i) a nonconstant CSM profile is needed to explain the PTF11qj radio light curves, and (ii) synchrotron cooling may be playing a role at late times. We also note that in Model 3, a flat ( $s = 0$ ) radial profile of the environment (interstellar medium (ISM)-like) is favored (see Chevalier 1982 for a discussion of the  $s = 0$  case). Finally, as shown in Figure 4, the combined radial evolution of the shock as implied by Model 0 for the first peak of the PTF11qj light curves and by Model 3 for the second peak implies that the shock has decelerated while encountering the CSM discontinuity. A similar case is of SN 2014C, where VLBI observations revealed that the SN has substantially decelerated at late times after encountering a higher-density shell (Bietenholz et al. 2021).

### 3.2. SSA Plus Off-axis GRB Scenario

Similarly to what was done in Palliyaguru et al. (2019), we also use numerical simulations for off-axis GRB jets by van Eerten et al. (2012) to model the second peak of the PTF11qj

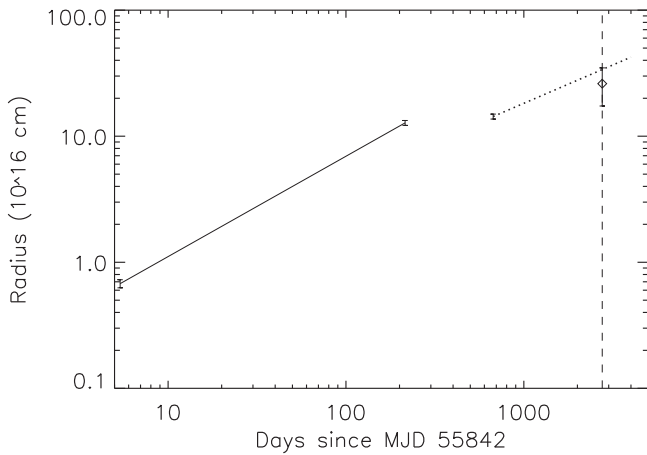


**Figure 4.** Radius vs. time during phases 1 and 2. During phase 2, the radial evolution is modeled using Model 3 in Table 3. The date of the 16 GHz VLBI data is marked by the vertical dashed line. The measured radius of  $(2.6 \pm 0.8) \times 10^{17}$  cm from the 15 GHz image is also indicated by a diamond. Our modeling does not include the time while encountering the CSM discontinuity and shows that the shock has decelerated during phase 2.

light curve within a constant-density environment, considering the new HSA and eMERLIN data points. Within this scenario, the first radio peak is the radio emission from the SN ejecta while the second radio peak is due to the delayed emission from an initially off-axis jet that enters our line of sight after spreading and decelerating. These two-dimensional hydrodynamic simulations of the GRB jets take into account the Blandford–McKee solution (Blandford & McKee 1976) in the relativistic regime, the Sedov–von Neumann–Taylor solution (Taylor 1950) in the late nonrelativistic regime, and a transition between regimes (Zhang & MacFadyen 2009).

In Table 4, we report the best-fit results for the isotropic equivalent kinetic energy of the explosion  $E_{\text{iso}}$ , the jet half-opening angle  $\theta_0$ , ISM density  $n_{\text{ISM}}$ , and the observer angle  $\theta_{\text{obs}}$ , when the latest four data points from HSA and eMERLIN, as well as the Chandra X-ray data point reported in Palliyaguru et al. (2019), are added to the fit. These fits also assume the equipartition of energy between particles and magnetic fields such that  $\epsilon_e = \epsilon_B = 0.33$ . We set the electron energy index,  $p = 2.5$ , which is typical for GRB afterglows, as expected from theoretical considerations (Kirk et al. 2000; Achterberg et al. 2001). The best-fit off-axis jet light curves are shown in Figure 2 (light blue, long-dashed lines).

### 3.3. Size Constraints: CSM-interacting versus Off-axis GRB Scenario

Within the SSA scenario, Models 0, 1, and 2 described in Section 3.1 all imply a shock radius around the time of the 16 GHz HSA observation (2759 days postexplosion) of  $r \sim 10^{18}$  cm. This in turn corresponds to an angular diameter of  $\sim 1$  mas at the redshift  $z = 0.028$  of PTF11qej, larger than the size constraints set by our HSA observations (see Table 1). On the other hand, Model 3 gives  $r \approx 3 \times 10^{17}$  cm at 2759 days postexplosion (see Figure 4), which corresponds to an angular diameter of  $\approx 0.4$  mas, compatible with the HSA observations reported in Table 1. We note, however, that within the SSA model, which assumes spherical symmetry, we are not able to model any potential asymmetry in the shock geometry.

Within the off-axis GRB scenario for the second radio peak, the ejecta will no longer produce a symmetric image on the sky.

Instead, the resolved image will highlight the front edge of the jet heading to the observer, producing an elongated and curved shape. For model 1 in Table 4, this curved front will have traveled  $R_{\perp, \text{travel}} = 3.0 \times 10^{19}$  cm in projected distance from the origin of the explosion. The projected width of the image is  $R_{\perp, w} = 1.4 \times 10^{19}$  cm, and its projected height  $R_{\perp, h} = 2.5 \times 10^{18}$  cm. These correspond to a projected angular distance from the origin of the explosion of 35 mas, a projected angular width of 8 mas, and a projected angular height of 14 mas. Thus, if the second radio light-curve peak of PTF11qej was due to an off-axis GRB, we should have resolved a much larger image in our HSA observations.

We note that while the off-axis GRB model considered here assumes a top-hat jet, a structured jet such as the one considered in Nakar & Piran (2017) would imply sizes that can be bracketed by the two extreme cases of a spherically symmetric blast wave, and a nonspreading relativistic cone. Indeed, for a spherically symmetric Sedov–Taylor blast wave, the analytical expression for the shock radius at a late time  $t$  is given by (van Eerten 2018)

$$R = C_R(k) \left( \frac{E_j}{10^{51} \text{ erg}} \right)^{\frac{1}{5-k}} \left( \frac{\rho_{\text{ref}}}{m_p} \right)^{-\frac{1}{5-k}} \times \left( \frac{R_{\text{ref}}}{c \times 10^6} \right)^{-\frac{k}{5-k}} \left( \frac{t}{10^8} \right)^{\frac{2}{5-k}}, \quad (14)$$

where  $C_R(k) = 1.5$  pc for the power-law index of the CSM density profile  $k = 1.4$  (Model 1, Table 3),  $E_j$  is the total energy in the ejecta, and  $\rho_{\text{ref}}$  and  $R_{\text{ref}}$  are the circumburst medium density and radius at a reference time (which we set to 10 days), respectively (van Eerten 2018). For the best-fit parameters of Model 1 in Table 3, we find the expected radius would be  $8.9 \times 10^{17}$  cm (1 mas), larger than our HSA constraint.

For a relativistic jet expanding into the ISM, the apparent radius at time  $t$  may be calculated using the analytical expression (Oren et al. 2004)

$$R_{\perp, \text{exp}} = 5 \times 10^{16} \left( \frac{E_{51}}{n} \right)^{1/6} T_j^{-1/8} t^{5/8}, \quad (15)$$

where  $T_j = (E_{51}/n)^{1/3} (\theta_0/0.1)^2 (1+z)$  is the jet break time,  $\theta_0$  is the jet half-opening angle, and  $n$  is the ISM number density (Oren et al. 2004). For the best-fit parameters of  $E_{\text{iso}}$ ,  $\theta_0$ , and  $n_{\text{ISM}}$  listed in Table 4, the expected radius at 2759 days postexplosion is  $4.8 \times 10^{19}$  cm. This corresponds to an angular size of  $\sim 55$  mas at the redshift  $z = 0.028$  of PTF11qej, much larger than our HSA constraint.

Based on these results, the off-axis hypothesis for the origin of the second radio peak of the PTF11qej light curves is disfavored.

## 4. Summary and Conclusion

We have presented HSA and eMERLIN observations of PTF11qej obtained  $\sim 7.5$  yr postexplosion. The source is marginally resolved in the HSA data at 15 GHz, indicating a diameter of  $(300 \pm 71) \mu\text{as}$ . This corresponds to an average expansion velocity of  $\approx 0.036c \pm 0.008c$ .

Modeling of the light curves within an SSA scenario requires the interaction of the shock with a nonsmooth CSM whose radial profile changes from a stellar wind profile ( $n_e \propto r^{-2}$ ) to a

**Table 4**  
Best-fit Results in the Off-axis GRB Scenario

| Model   | $E_{\text{iso}}$   | $n$                  | $\theta_0$ | $\theta_{\text{obs}}$ | $p$ | $\chi^2$             | $R_{\perp}$          | Angular Size | $R_{\perp, \text{exp}}$ | Expected Angular Size |
|---------|--------------------|----------------------|------------|-----------------------|-----|----------------------|----------------------|--------------|-------------------------|-----------------------|
|         | (erg)              | ( $\text{cm}^{-3}$ ) | (rad)      | (rad)                 |     |                      | (cm)                 | (mas)        | (cm)                    | (mas)                 |
| Model 1 | $1 \times 10^{53}$ | $1 \times 10^{-5}$   | 0.2        | 0.4                   | 2.5 | $1285/41 \approx 31$ | $3.0 \times 10^{19}$ | 35           | $4.8 \times 10^{19}$    | 55                    |

**Note.** The radius ( $R_{\perp}$ ) and the corresponding angular diameter from modeling, and the expected radius from Equation (15) ( $R_{\perp, \text{exp}}$ ), and the corresponding angular diameter are also listed.

constant-density medium. This variable CSM profile also affects the temporal evolution of the shock radius. We also find that synchrotron cooling may be playing a role at the highest radio frequencies. Within this SSA model with variable CSM, the derived size of the shock at the time of our HSA observations can be reconciled with our measurements. Our results are thus consistent with the CSM interaction model (considering that such model is highly simplified). The size constraints derived from our HSA observations also seem to disfavor an off-axis relativistic jet scenario for the radio rebrightening of PTF11qcj.

In conclusion, the VLBI observations reported in this paper favor the original interpretation of PTF11qcj as a strongly CSM-interacting radio SN (see Corsi et al. 2014; Palliyaguru et al. 2019). However, our conclusions are limited by the simplifications inherent in the spherically symmetric SSA model adopted here. We encourage more detailed theoretical modeling aimed at interpreting the complex radio light curve of and available VLBI data on PTF11qcj.

A.C. acknowledges support from the National Science Foundation CAREER Award #1455090, and from Chandra GO Award #GO7-18065X. N.T.P. acknowledges support from NSF NANOGrav Physics Frontier Center (NSF grant No. PFC-1430284) and start-up funds to J.D. Romano from TTU. M.P.-T. acknowledges financial support from the State Agency for Research of the Spanish Ministry of Science, University, and Education (MCIU) through the ‘‘Center of Excellence Severo Ochoa’’ award for the Instituto de Astrofísica de Andalucía (SEV-2017-0709) and through grants AYA2015-63939-C2-1-P and PGC2018-098915-B-C21. The National Radio Astronomy Observatory is a facility of the National Science Foundation operated under cooperative agreement by Associated Universities, Inc. eMERLIN is a National Facility operated by the University of Manchester at Jodrell Bank Observatory on behalf of STFC. This work made use of the Swinburne University of Technology software correlator, developed as part of the Australian Major National Research Facilities Programme and operated under license.

#### ORCID iDs

N. T. Palliyaguru  <https://orcid.org/0000-0002-4828-0262>  
A. Corsi  <https://orcid.org/0000-0001-8104-3536>  
M. Pérez-Torres  <https://orcid.org/0000-0001-5654-0266>  
E. Varenius  <https://orcid.org/0000-0002-3248-9467>  
H. Van Eerten  <https://orcid.org/0000-0002-8680-8718>

#### References

- Achterberg, A., Gallant, Y. A., Kirk, J. G., & Guthmann, A. W. 2001, *MNRAS*, **328**, 393
- Berger, E., Kulkarni, S. R., Frail, D. A., & Soderberg, A. M. 2003, *ApJ*, **599**, 408
- Bietenholz, M. F., Bartel, N., Kamble, A., et al. 2021, *MNRAS*, **502**, 1694
- Blandford, R. D., & McKee, C. F. 1976, *PhFl*, **19**, 1130
- Cano, Z., de Ugarte Postigo, A., Pozanenko, A., et al. 2014, *A&A*, **568**, A19
- Chevalier, R. A. 1982, *ApJ*, **258**, 790
- Chevalier, R. A. 1998, *ApJ*, **499**, 810
- Chevalier, R. A., & Fransson, C. 2003, in *Supernova Interaction with a Circumstellar Medium*, ed. K. Weiler, Vol. 598 (Berlin: Springer-Verlag), 171
- Chevalier, R. A., & Fransson, C. 2006, *ApJ*, **651**, 381
- Chevalier, R. A., Li, Z.-Y., & Fransson, C. 2004, *ApJ*, **606**, 369
- Corsi, A., Gal-Yam, A., Kulkarni, S. R., et al. 2016, *ApJ*, **830**, 42
- Corsi, A., Ofek, E. O., Gal-Yam, A., et al. 2014, *ApJ*, **782**, 42
- Deller, A. T., Brisken, W. F., Phillips, C. J., et al. 2011, *PASP*, **123**, 275
- Filippenko, A. V. 1997, *ARA&A*, **35**, 309
- Galama, T. J., Vreeswijk, P. M., van Paradijs, J., et al. 1998, *Natur*, **395**, 670
- Gal-Yam, A. 2017, in *Observational and Physical Classification of Supernovae*, ed. A. W. Alsabti & P. Murdin (Berlin: Springer), 195
- Greisen, E. W. 2003, *Information Handling in Astronomy—Historical Vistas*, Vol. 285 (Dordrecht: Kluwer), 109
- Hjorth, J., & Bloom, J. S. 2012, in *The Gamma-Ray Burst—Supernova Connection*, ed. C. Kouveliotou et al., Vol. 51 (Cambridge: Cambridge Univ. Press), 169
- Ho, A. Y. Q., Goldstein, D. A., Schulze, S., et al. 2019a, *ApJ*, **887**, 169
- Ho, A. Y. Q., Phinney, E. S., Ravi, V., et al. 2019b, *ApJ*, **871**, 73
- Kettenis, M., van Langevelde, H. J., Reynolds, C., & Cotton, B. 2006, in *ASP Conf. Ser. 351, Astronomical Data Analysis Software and Systems XV*, ed. C. Gabriel et al. (San Francisco, CA: ASP), 497
- Kirk, J. G., Guthmann, A. W., Gallant, Y. A., & Achterberg, A. 2000, *ApJ*, **542**, 235
- Kulkarni, S. R., Frail, D. A., Wieringa, M. H., et al. 1998, *Natur*, **395**, 663
- Li, Z.-Y., & Chevalier, R. A. 1999, *ApJ*, **526**, 716
- Margutti, R., Metzger, B. D., Chornock, R., et al. 2019, *ApJ*, **872**, 18
- Mészáros, P. 2006, *RPPh*, **69**, 2259
- Modjaz, M., Liu, Y. Q., Bianco, F. B., & Graur, O. 2016, *ApJ*, **832**, 108
- Moldon, J. 2018, in *14th European VLBI Network Symp. & Users Meeting (EVN 2018) (Trieste: PoS)*, 152
- Nakar, E., & Piran, T. 2017, *ApJ*, **834**, 28
- Offringa, A. R., McKinley, B., Hurley-Walker, et al. 2014, *MNRAS*, **444**, 606
- Oren, Y., Nakar, E., & Piran, T. 2004, *MNRAS*, **353**, L35
- Palliyaguru, N. T., Corsi, A., Frail, D. A., et al. 2019, *ApJ*, **872**, 201
- Piran, T. 2004, *RvMP*, **76**, 1143
- Rivera Sandoval, L. E., Maccarone, T. J., Corsi, A., et al. 2018, *MNRAS*, **480**, L146
- Rybicki, G. B., & Lightman, A. P. 1986, *Radiative Processes in Astrophysics* (New York: Wiley)
- Salas, P., Bauer, F. E., Stockdale, C., & Prieto, J. L. 2013, *MNRAS*, **428**, 1207
- Smartt, S. J., Clark, P., Smith, K. W., et al. 2018, *ATel*, **11727**, 1
- Soderberg, A. M., Chakraborti, S., Pignata, G., et al. 2010, *Natur*, **463**, 513
- Soderberg, A. M., Kulkarni, S. R., Berger, E., et al. 2005, *ApJ*, **621**, 908
- Soderberg, A. M., Nakar, E., Berger, E., & Kulkarni, S. R. 2006, *ApJ*, **638**, 930
- Taylor, G. 1950, *RSPSA*, **201**, 159
- van Eerten, H. 2018, *IJMPD*, **27**, 1842002
- van Eerten, H., van der Horst, A., & MacFadyen, A. 2012, *ApJ*, **749**, 44
- Woosley, S. E., & Bloom, J. S. 2006, *ARA&A*, **44**, 507
- Zhang, W., & MacFadyen, A. 2009, *ApJ*, **698**, 1261